Microphysical view of development and ice production of mid-latitude stratiform clouds with embedded convection during an extratropical cyclone

Yuanmou Du[1,3], Dantong Liu[2], Delong Zhao[1,3], Mengyu Huang[1,3], Ping Tian[1,3], Dian Wen[1,3], Wei Xiao[1,3], Wei Zhou[1,3], Baiwan Pan[2], Dongfei Zuo[4], Xiange Liu[1,3], Yingying Jing[1,3], Rong Zhang[4], Jiujiang Sheng[1,3], Fei Wang[1,3], Yu Huang[1,3], Yunbo Chen[1,3], Deping Ding[1,3]

[1]Beijing Weather Modification Center, Beijing, 100089, China
[2]Department of Atmospheric Sciences, School of Earth Sciences, Zhejiang University, Hangzhou, Zhejiang, 310027, China
[3]Beijing Key Laboratory of Cloud, Precipitation and Atmospheric Water Resources, Beijing, 100089, China
[4]CMA Weather Modification Center, Beijing, 100081, China

Correspondence to: dantongliu@zju.edu.cn

Abstract. The microphysical properties associated with the ice production importantly determine the precipitation rate of clouds. In this study, the microphysical properties including the size distribution and particle morphology of water and ice for stratiform clouds with embedded convection during an extratropical cyclone over the northern China were in-situ characterized. Stages of cloud were investigated including young cells rich of liquid water, developing and mature stages with high number concentration of ice particles (N_{Ice}). The N_{Ice} could reach 300 L^{-1} at the mature stage, about two orders of magnitudes higher than the primary ice number concentration calculated from ice nucleation. This high N_{Ice} occurred at about −5 to −12 ºC, spanning the temperature region of Hallett-Mossop process and possible other mechanisms for the secondary ice production (SIP). The N_{Ice} was positively associated with the number concentrations of graupel with diameter (d) > 250 μm and large supercooled droplet (d > 50 μm). The SIP rate was 0.005-1.8 L^{-1}s^{-1} derived from the measured N_{Ice} with known ice growth rate between two sizes. The SIP rate could be produced by a simplified collision-coalescence model within an uncertainty factor of 5, by considering the collection of large droplets by graupel. The collection efficiency between the graupel and droplet was found to increase when the size of droplet was closer to graupel which may improve the agreement between measurement and model. Importantly, the overall N_{Ice} was found to be highly related to the distance to cloud-top (DCT). The level with larger DCT had more abundant rimmed graupels falling from the above level, which promoted the coalescence processes between graupels and droplets, producing a higher fraction of smaller ice through SIP. This seeder-feeder process extended the avalanche SIP at lower temperature up to −14 ºC beyond the temperature region of Hallett-Mossop process. The results illustrated the microphysical properties of clouds with convective cells under different stages, which will improve the understanding of the key processes in controlling the cloud glaciation and precipitation process.

1 Introduction

The mid-latitude clouds are mostly present in mixed-phase (Mülmenstädt et al., 2015). The microphysical properties associated with the ice production or the conversion from liquid water to ice importantly determine the precipitation rate and lifetime of clouds (Lau and Wu, 2003; Cantrell and Heymsfield, 2005). The growth rate of hydrometeors through the ice phase is usually more rapid than the warm rain process (Lohmann and Feichter, 2005; Mcfarquhar et al., 2017). Understanding the ice production and glaciation process in clouds is important for more accurate parameterization of microphysical processes in weather prediction models (Korolev et al., 2017; Bacer et al., 2021), and this needs to be understood in vertical dimension and under different stages of cloud development (Zhao et al., 2019) .

In addition to the primary ice produced by homogeneous and heterogeneous nucleation processes from aerosol particles (Kanji et al., 2017), the secondary ice production (SIP) process can rapidly produce high numbers of ice up to several orders of magnitude more than that produced from ice nucleation (Mossop, 1985; Harris-Hobbs and Cooper, 1987; Field et al., 2016; Korolev et al., 2022), which is an important process to accelerate the cloud glaciation. The SIP can occur under different ambient temperatures through different processes including the rime splintering process, fragmentation during droplet freezing, fragmentation due to ice–ice collision, ice particle fragmentation due to thermal shock, fragmentation of sublimating ice particle, and the activation of ice-nucleating particles in transient supersaturation around freezing drops (Korolev et al., 2020). The Hallett-Mossop (H-M) mechanism was well reproduced through laboratory work (Hallett and Mossop, 1974) and is usually introduced to explain the high abundance of ice number concentration at slightly sub-freezing temperature (−3 to −8 °C) (Hogan et al., 2002; Huang et al., 2008; Crosier et al., 2013; Korolev et al., 2022), and the freshly formed ice mostly exhibited the shapes of columns or needles (Locatelli et al., 2008; Crosier et al., 2011; Lloyd et al., 2014; Taylor et al., 2016), consistent with the diffusion growth habit of ice under such temperature. However, the H-M process may not sufficiently explain the even more rapid SIP rate in observation, the fragmentation during droplet freezing and ice-ice collision may play an important role in the secondary ice production process (Rangno and Hobbs, 2001), it may also be formed by the growth of ice from the outside into the H-M temperature zone (Field et al., 2016). Supercooled large drop may play important roles in the SIP process, which can fracture when freezing and emit ice splinters (Lawson et al., 2015), and this process could extend the SIP to a lower temperature under the influence of strong updraft. A recent study also found SIP process could occur at temperature as low as −27 °C (Korolev et al., 2022).

Mid-latitude clouds formed from extratropical cyclone are the main sources of precipitations for the east Asia (Li et al., 2016). The microphysical properties of clouds over the North China Plain have been observed during frontal systems (Yang et al., 2017; Hou et al., 2021; Hou et al., 2023). It was found more ice particles close to the convective region and the SIP was found to produce ice number concentration up to over 300 L^{-1}, which may promote the intensity of precipitation. These studies suggest that the SIP process may be explained by the H-M process or other mechanisms, such as collisional fragmentation, which may contribute to SIP in regions that do not fit the H-M criteria (Hou et al., 2023). However, the key

65 factors in controlling the SIP process and how these factors can influence the SIP at different stages of clouds have not been elucidated.

The cold front system formed by the merging of cold air from the rear of extratropical cyclones with the warm air mass brought in by the southwest warm and moist air along the edge of the subtropical high-pressure system is the main weather system that produces rainfall in northern China (Wang et al., 2014). This study therefore investigated the microphysical

70 properties of a typical mid-latitude cloud formed via this typical weather system over the North China Plain through aircraft in-situ measurements. Stages of cloud were investigated including young cells rich of liquid water, developing and mature stages with high number concentration of ice particles. The key factors in controlling SIP are elucidated through the calculation from measurements and modelling.

2 Experiment

75 ### 2.1 Instrumentation

The Kingair350 aircraft of Beijing weather modification center was employed for in-situ measurements in this experiment (Liu et al., 2020; Tian et al., 2020; Zuo et al., 2023). This experiment aimed to conduct continuous aircraft observations of clouds developed during an extratropical cyclone over northern China. The goals were to obtain in-situ microphysical data of clouds during the development of frontal system and to study the production of ice in clouds. The experiment was designed

80 based on numerical model forecasting results and real-time radar data. To capture the microphysical characteristics of stratiform clouds with embedded convection at various development stages, aircraft observational experiment was conducted in accordance with real-time changes in precipitation radar echoes.

The air temperature was measured by Rosemount total-air temperature probe (Lenschow and Pennell, 1974; Lawson and Cooper, 1990). The temperature may be underestimated due to water evaporation however this artifact is negligible for

85 supercooled clouds (Lawson and Rodi, 1992; Korolev and Isaac, 2006), and the temperature shift in and out of clouds was not observed in this study. The wind speed and wind direction were measured by Aircraft Integrated Meteorological Measurement System (AIMMS20, Aventech Research Inc.) with a time resolution of 1 second (Beswick et al., 2008). The distribution of aerosol particles ranging from 0.1 to 3 µm in diameter was measured by Passive Cavity Aerosol Spectrometer Probe (PCASP, DMT Inc.) with a time resolution of 1 second (Cai et al., 2013).

90 The Fast Cloud Droplet Probe (FCDP, SPEC inc.) (Lance et al., 2010) was used to measure cloud droplets with a diameter range of 2-50 µm and a resolution of about 3 µm. It resolves the particles into 20 size bins, and the optical sizing was calibrated with known-sized standard glass beads. The liquid water content (LWC) at diameter of 2-50 µm was calculated by integrating the volume at all size bins by the FCDP (Lu et al., 2012). Two-dimensional stereoscopic optical array imaging probe (2D-S, SPEC Inc.) was used to record images of cloud particles and provide the size, shape and concentration of

95 particles. 2D-S has two orthogonal laser beams that cross in the middle of the sample volume and casts the shadowgraph of particles on two linear 128-photodiode arrays when the particles transit through the laser (Lawson et al., 2006). It can

measure particles of 10-1280 μm in diameter with a resolution of 10 μm, and provide detailed information of different phase particles in cloud. The precipitation particle was measured by High Volume Precipitation Spectrometer (HVPS, SPEC Inc.) (Lawson et al., 1998), which is also an imaging array probe with a measure range and resolution of 150-19200 μm and 150 μm respectively. The laser beam of HVPS illuminates the imaging system, and records shadow images on the 128 elements linear photodiode array when particles pass through the sample volume. The S-band weather radar located in Beijing (Jiang and Liu, 2014) was used to help analyze the macroscopic characteristics of cloud, which can detect targets within a radius of 230 km with a time and radial spatial resolution of 6 minutes and 1 km, respectively. The distance from the radar to the observed cloud system in this study was approximately 50-200 km.

The Optical Array Shadow Imaging Software was used to process the raw data of 2D-S and HVPS, which can distinguish liquid drop and ice particle according to the circularity of particles (C) (Crosier et al., 2011). The C is calculated from Eq. (1):

$$C = \frac{P^2}{4\pi A},\qquad(1)$$

where P and A are the perimeter around the edge of the particle and total area of the particle respectively. The perfect sphere has circularity of 1, and the other shapes have larger circularity. Irregular particles with larger circularity are counted as ice particles because the shape of ice is unlikely to be round. Considering the poorly imaged or distorted large drops/drizzles may be counted as ice particles, the circularity threshold for ice particles (irregular class) is raised to 1.2. Calculated circularity values may also be less than 1 due to the presence of images composed of only a small number of pixels, so the low threshold for water drops (round class) is reduced to 0.9. In practical terms, particles with an area less than 20 pixels are classified as the small class because it is difficult to determine the shape with few pixels, and particles with an area more than 20 pixels are classified as round class ($0.9 \leq C < 1.2$) or irregular class ($C \geq 1.2$). The round and irregular class are regarded as liquid drop and ice particle, respectively. The round class is large droplet with a diameter larger than 50 μm, and it was represented by large droplet in this study to distinguish from the cloud droplets (2-50 μm) measured by the FCDP.

The shapes of irregular ice particles were further clarified into five habit classes including linear, plate, irregular, aggregate and dendrite, according to the maximum dimension, width, linearity, circularity and density of particles (Zhang et al., 2021). The mass of ice was determined by particle shapes according to the approximate mass formulas for ice particles (Holroyd, 1987), and hereby the ice water content (IWC) was calculated, and the total water content (TWC) was obtained. It should be noted that the error in calculating ice mass according to the mass-dimension relationship will increase when ice particle is larger and the shape has large irregularity to be classified (Crosier et al., 2013).

The concentration of ice nucleating particles (INP) in study was calculated by the parameterization relationship (Demott et al., 2010), which is expressed as:

$$n_{\mathrm{IN},T_k} = a(273.16 - T_k)^b (n_{\mathrm{aer},0.5})^{(c(273.16-T_k)+e)},\qquad(2)$$

Where $a = 0.0000594$, $b = 3.33$, $c = 0.0264$, $e = 0.0033$. n_{IN,T_k} is the number concentration of INP (L^{-1}), and T_k is the temperature of cloud in degrees Kelvin, and $n_{\mathrm{aer},0.5}$ is the number concentration of aerosol particles with diameter larger than

0.5 μm. and $n_{aer,0.5}$ is the number concentration of aerosol particles with diameter larger than 0.5 μm. In this study, $n_{aer,0.5}$ measured by PCASP at the cloud base was used for calculation.

2.2 Overview of experiment

On 26th September 2017, light precipitation occurred in North China under the influence of eastward moved upper trough. ERA5 reanalysis data at 08:00 BJT (UTC+8h) with a resolution of 0.25 degrees from European Centre for Medium-Range Weather Forecasts (ECMWF) showed there was a deep cold vortex system in the northwest of East Asia at 500 hPa (Fig. 1a), the bottom of which split into the shortwave trough and moved eastward, leading to a southward moved cold advection at the middle-level and conditional instability stratification (Fig. S1). Figure 1b showed the existence of a convergence zone at 850 hPa, where a cold front was located, and sufficient water vapor was transported through the prefrontal southerly wind. The abundance of water vapor and upward motion of air led to the generation of a series of stratiform clouds, and convective clouds also appeared under the condition of instability stratification.

The study region in this research was Zhangjiakou, Hebei Province (northwest of Beijing) and Beijing, and aircraft departed from the airport in northern Beijing at 09:54 BJT and flew to Zhangjiakou. The precipitation mainly occurred in Zhangjiakou and became weaker after 11:00 BJT on 26th September 2017, then the precipitation band gradually moved to Beijing, and weather stations observation data indicated the precipitation rate during this experiment were generally less than 1 mm/h. Figure S2 shows the movement of the surface cold front, i.e., the convergence zone of cold and warm air masses at the surface as determined by the temperature and wind shear measured by the ground sites. The center of the extratropical cyclone was located in Outer Manchuria (Fig. S3), and the surface cold front extended southwestward from the position of the extratropical cyclone to the experimental region, the experimental region was situated within the trailing end of the cold front cloud system, which extended southward from the extratropical cyclone cloud system. At 09:00 to 12:00 BJT, the surface cold front continued to move southeastward and lifted the warmer and moist air mass in front. The warm air mass ascended along the front, forming clouds and precipitation, and the aircraft observation area was situated behind the cold front. The aircraft sampled the clouds formed in this cyclonic system at this stage, i.e. behind the surface cold front line (Fig. S3) and for the newly formed, developing and matured clouds. This is the typical cloud system formed in this extratropical weather system over the northern China.

3 Results and discussion

3.1 Identifying stages of cloud development

Four relative stages during the lifecycle of clouds were identified during experiment, which corresponded to the developing (P1), mature (P2), dissipating (P3) and young cells (P4) in cloud system, according to the different glaciation extents of clouds. The ice mass fraction (F_{Ice}: IWC/TWC) was used to indicate the different development stages of clouds (Fig. 2), by considering a more mature cloud has a more glaciated fraction, for the discussions of cloud microphysics at different stages.

160 The cloud system was formed through the combined effects of dynamic forcing induced by the frontal uplift and the moisture transport provided by the prefrontal southerly air mass. Therefore, this study postulated that the continuous clouds within the cloud system had similar dynamic and thermodynamic properties. Aircraft performed flight altitudes of 3.2-5.7 km in P1, 5.2-5.8 km in P2, 4.9-5.2 km in P3 and 2.1-4.9 km in P4, and AIMMS data indicated that the 0 °C layer was at about 3.4 km. The flight tracks mapping on the composite reflectivity of precipitation radar are shown in Fig. 3, colored by

165 the LWC from FCDP and IWC from 2D-S respectively, the radar times and the flight time windows for the four stages are shown in Table S1. In developing cells, substantial LWC was detected up to 0.3 g m^{-3}, and the aircraft penetrated a high IWC region in this cloud at 10:09-10:11 BJT, with the highest IWC exceeded 2 g m^{-3} (Fig. 3a1, b1), and F_{Ice} at this stage could span from zero (pure water) to unit (pure ice) (Fig. 2). In mature cells, F_{Ice} ranged in 0.36-1 and IWC generally exceeded 0.3 g m^{-3} (Figs. 2 and 3b2), and the maximum radar reflectivity of mature cells was enhanced from 20 dBZ to 27

170 dBZ at 10:06 to 10:42 BJT (Fig. 3a1, a2). At the dissipating stage, the ice phase precipitation process occurred and the radar reflectivity became weaker with narrowed cloud band (Fig. 3a3, b3), and the range of F_{Ice} reached up to 0.56-1 (Fig. 2). The last stage was young cells with lower glaciated fraction (Fig. 2), the rich liquid water produced from the newly developed thermals after the front cloud bands dissipated (Fig. 3a4, b4).

Figure 4 shows the microphysical properties of clouds and meteorological parameters along the flight track, and Figure 4

175 is broken into four figures according to four stages with shorter time window showing finer details (Fig. S4). The vertical wind data during aircraft turns were excluded from Figs. 4 and S4 and were not used for the analysis. The cross section of radar reflectivity in Fig. 4a can provide information about the relative positions of aircraft with respect to the cloud top and base, as well as the echo intensity of the cloud. The cross section of radar reflectivity along the flight track was calculated based on the aircraft position. A vertical line was first determined according to the latitude and longitude of the aircraft, then

180 the azimuth angles, elevation angles, and range bins of equidistant points with a resolution of 30 meters in the vertical line were obtained, and the radar reflectivity of each equidistant point was calculated by linear interpolation in nearest neighbor combined with a vertical direction (NVI) method. The cloud-top height is indicated by red line on the radar profile, where the areas with radar reflectivity factor more than or equal to 5 dBZ were considered as cloud, and other areas were considered as clutter. This might give a lower estimation for the height of cloud-top because the rain radar was only sensitive

185 to clouds with precipitation, but might not efficiently detect clouds dominated by liquid water. The size spectrum of ice showed a bimodal mode with a minima diameter (d) at 180 μm (Fig. S5). The sensitivity was tested by altering the threshold from 160-200 μm, and the resultant difference of smaller ice fraction was within 10%. The fraction of smaller ice with $d <$ 180 μm ($F_{smaller\ ice}$) was defined to imply the freshly formed smaller ice which had not experienced sufficient growth (Fig. 4b).

190 P1 was strongly turbulent with vertical wind speed up to 8.9 m/s, and the strong updraft region was dominated by ice particles and precipitation particles (Fig. 4c-e). The low LWC when high vertical updraft may be caused by the rapid production of ice particles, which was also observed in tropical highly convective region (Lawson et al., 2015). The ice number peaked at a valley between two peaks of liquid water, but it was difficult to determine the vertical wind at the peak

of ice number due to aircraft turns (Fig. S4). However, in the subsequent level flight, high ice number concentration (> 170 L^{-1}) was also observed in the strong updraft region. After the high ice number region, LWC up to 0.28 g m^{-3} was observed in the region with weaker updraft.

The cloud-top height in P2 reached 10 km (Fig. 4a), which was the highest cloud-top of clouds observed during experiment. The LWC in P2 was considerably lower compared to P1, while there were more large droplets and ice particles in clouds (Fig. 4d, e), and the distribution of large droplets and ice particles in P2 showed a bimodal distribution. The strength of turbulence in P2 was weaker than P1 (Fig. 4c), but P2 was more glaciated than P1 with F_{Ice} spanning from 0.36 to 1 (Fig. 2). P3 and P4 were relatively quiescent compared to other stages. The cloud-top height in P3 was lower than P2, and the area of stronger echoes (>20 dBZ) was also reduced compared to P2 (Fig. 4a). Similar to P2, the dissipating stage was dominated by ice but only intermittent unglaciated LWC-rich clouds were present (Fig. 4d, e), however, the clouds in P3 had a more glaciated fraction (Fig. 2). All above confirmed the dissipating stage of P3. P4 was likely a newly developed cell with lower F_{Ice} and weak radar reflectivity, and the cloud-top had not reached as high as other stages (Figs. 2 and 4a). This stage was rich of liquid water with LWC up to 0.27 g m^{-3} at a colder temperature (−11 ºC), while there was no appreciable IWC measured in the region (Fig. 4d, e).

Figure 5 summarizes the relation between LWC and IWC at different stages of cloud development. For the newly developed cell (P4), the high LWC with less IWC (< 0.2 g m^{-3}) was predominant, and this feature was also present at developing stage. The other stages with appreciable IWC corresponded with LWC less than 0.2 g m^{-3}, indicating the clouds with different extents of glaciation. The clouds in P2 were primarily composed of ice water, with the number concentration of cloud droplets significantly lower compared to P1. P3 was identified as dissipating cells, when the clouds were dominated by ice water, and had a higher F_{Ice} than P2 (Fig. 2).

The MODIS level 2 standard product (MYD06) at 10:30 BJT (Fig. S6) showed the distribution of cloud optical depth in the study region was almost opposite to the cloud effective radius, and the area with high value of cloud optical depth corresponded to a lower cloud-top temperature, which was consistent with the distribution of precipitation. The lower cloud optical depth and cloud-top temperature in Zhangjiakou area suggested the lower water content and higher cloud-top height of the cloud region. There were still large hydrometeors in cloud that had not formed precipitation, thus the cloud effective radius in Zhangjiakou area was larger. The satellite results were also consistent with the different stages of the clouds identified based on in-situ data. According to the flight tracks of aircraft at different stages of clouds (Fig. 3), it was observed that during the developing stage, the cloud exhibited high optical depth and small effective radius, and a warmer cloud-top temperature (Fig. S6). In mature cells, there was a noticeable decrease in cloud-top temperature, and due to precipitation occurrence, the optical depth decreased while the effective radius increased. In dissipation cells, as the cloud-top height decreased and the cloud-top temperature became warmer, both the optical depth and effective radius in this region decreased, indicating the dissipation of cloud.

3.2 Ice production at different stages of cloud development

Figure 6 shows the vertical profiles of microphysical properties at different stages. Figure 6a1-a4 and 6c1-c4 are colored by the effective diameter of droplets and $F_{smaller\ ice}$, respectively. Several targeting periods of P1, P2, and P4 were selected for detailed analysis, including periods 1.1, 1.2, 2.1, 2.2, 2.3, 4.1, 4.2, 4.3 (specific times are given in Table S1), and the corresponding periods are marked in the time series of Fig. 4. In developing cells, N_{FCDP} tended to decrease with the increase of height, while the diameter of droplets tended to increase (Fig. 6a1), and there was an increase in N_{Round} at two levels. The broadened droplet spectrum at two levels of developing cells was also observed (Fig. S5). The period 1.1 (abbreviated as P1.1, the same for other periods) corresponded to high concentrations of ice (N_{Ice}) with less LWC, and P1.2 corresponded to the region with less ice and some LWC (Fig. 6c1). The size spectrum in Fig. 7a showed the N_{FCDP} and $F_{smaller\ ice}$ at P1.2 were both higher than P1.1, and precipitation particles had formed at P1.1, whereas P1.2 was still dominated by smaller droplets with few precipitation particles (Fig. 6d1). Clear similarities were observed between the two periods: the N_{round} in both periods was higher than other unmarked periods in P1, and the average N_{Round} exceeded 30 L^{-1} (Fig. 7a), with the maximum N_{Round} was over 50 L^{-1} (Fig. 6b1). In addition, the larger size determined by the 2D-S than FCDP was found in Fig. 7, which was due to the lower accuracy for 2D-S to determine the particles in smaller bins (Gurganus and Lawson, 2018; Woods et al., 2018). This may be particularly the case when some small non-spherical ices were present at colder temperatures.

P1.1 and P1.2 showed N_{Ice} up to 256 L^{-1} and 71 L^{-1} respectively, by considering the factor of 10, which is the uncertainty point out by Demott et al. (2010), the observed ice concentration was still about 2 orders of magnitude higher than the calculated INP in the corresponded temperature regime (Fig. S7). The ice shapes showed to be dominated with plate, irregular and linear ice (Fig. 7a), and the 2D-S images showed the presence of H-shaped ice crystals, and the ice particles exhibited obvious riming characteristic. The ice habits were consistent with the feature of cloud region where SIP is thought to be active (Field et al., 2016), considering the temperature of the environment was within the H–M zone, and the region was rich in supercooled large droplets, the H-M process was most likely active (Crosier et al., 2013; Taylor et al., 2016). The ice production of P1.1 and P1.2 appeared to be triggered by the riming process of large ice particles, and the temperature of two periods also indicated the likely H-M process for SIP during this stage (Fig. 7a). The difference between the two periods was that P1.1 seemed to have completed the SIP process and formed precipitation particles, while there was still a large number of cloud droplets at P1.2 with smaller number of large ice. This might suggest the great number of large ice at P1.1 improved the riming efficiency and increased the riming surface area, leading to more small ice through H-M process and resulting in the consumption of the droplets. However, the dynamic vertical or horizontal transported of produced ice might induce some uncertainty when evaluating the concentration at the supposed same aircraft position.

Cloud-top height developed to 10.1 km in mature cells, and the temperature at this stage was lower than the H-M temperature regime. P2.1, P2.2 and P2.3 corresponded to areas with high, modest, low concentration of ice in P2, respectively, the N_{Round} decreased gradually from P2.1 to P2.3, and P2.2 had more cloud droplets (Fig. 6a2-d2). The size spectrum in Fig. 7b showed that the N_{Ice}, N_{Round} and $F_{smaller\ ice}$ at P2.1 were all higher than that at P1.1. The plate, irregular

and linear ice also accounted for the majority of ice at P2.1, and the riming characteristic of large ice at P2.1 was clearly
shown in the images (Fig. 7b). Although the average temperature of P2.1 was as low as −11.7 °C, the abundant large ice
particles triggered the active SIP process at P2.1 with high N_{Ice} about 300 L^{-1}, indicating that the SIP process was not
restricted by temperature. The period 2.2 that lacked enough large ice was still in the glaciation process, and P2.3 was
difficult to trigger a more active SIP process with smaller number of large ice and liquid water.

In dissipating cells, the clouds were dominated by ice and $F_{smaller\ ice}$ decreased, indicating the ice production process had
completed (Fig. 6a3-d3). The clouds in P4 were dominated by liquid water and classified as young cells, the cloud-top of P4
was only 5.5 km (Fig. 6a4-d4). The vertical profiles showed that P4.1 and P4.3 were dominated by droplets with few ice
particles and large droplets, while P4.2 was composed of large droplets with few droplets. The ice particles observed at this
stage most likely originated from the ice nucleating process and the ice falling from above. Aircraft penetrated the cloud-top
at P4.3, where several primary ice particles could be observed (Fig. 7c). The size spectrum and 2D-S images in Fig. 7c
showed that large ice presented at P4.1, and ice grew through riming and Bergeron processes, while the ice at P4.2 was
mainly smaller ice, which was still in the process of growth.

The large ice falling from the upper layer played a very important role in ice production process, the primary ice crystals
formed through the nucleation process and grew up in the upper layer or during the fall, then fell to the lower layer to trigger
the ice production process. However, the number of large ice particles was not the only factor that determined the ice
production process, the large droplet also played a significant role in promoting the SIP process. Figure 8 shows the scatter
plots of the corresponding distribution of N_{Ice} and N_{Round} at different stages, colored by the diameter of large droplet. There
was a positive correlation between N_{Ice} and N_{Round}, where more large droplets generally corresponded to a higher N_{Ice}.
Comparing P1.1 and P1.2, it could be found that the larger large droplet tended to produce a higher N_{Ice} at the same N_{Round},
the large droplet with a diameter of 160 μm corresponded to almost 5-folds ice numbers of that of 80 μm, and Figure 8 also
clearly showed the importance of the larger large droplet to produce more ice particles in P2. Based on the above analysis, it
could be inferred that when a high number of large ice particles fell from the upper layer to the lower layer, if there were
abundant larger large droplets in the lower layer, the riming efficiency could be improved, and then the SIP process could be
enhanced.

3.3 Ice production determined by the distance to cloud-top

Figure 4 showed even at the same level, N_{Ice} had two orders of magnitude difference from less than unit to a few hundred per
litre. This means during the aircraft penetration, the different intensity of SIP events had been experienced. The main reason
causing this variability was attributed to the position of aircraft relative to the cloud-top, i.e. the distance to cloud-top (DCT)
for the measurement.

Figure 4b shows the time series of DCT during experiment. When penetrating a cloud turret, aircraft entered the cloud
with a low DCT, reaching a higher DCT when close to convective core, leaving the cloud with a low DCT again. It therefore
showed a few humps of DCT during a few penetrations of convective cells or more spread part of clouds. The DCT ranged

from 0.01 to 4.6 km during the experiment. Figure 4b and d showed the higher DCT (2.8 and 4 km, respectively) corresponded to the peak values of N_{Ice} (256 and 300 L^{-1}, respectively) in P1 and P2. For each penetration, N_{Ice} increased dramatically when aircraft was closer to the cloud core with higher DCT, but reduced when leaving. This clearly indicated the positive correlation between DCT and N_{Ice}.

Figure 9 shows N_{Ice} and N_{FCDP} as a function of DCT for different stages of clouds. At the developing stage, N_{Ice} significantly enhanced when DCT was above 2km, and was positively correlated with N_{Ice} up to DCT of 3km. For the mature and dissipating stage, N_{Ice} was enhanced from the cloud-top (DCT = 0.2 km) to a certain DCT but decreased when larger DCT. This suggested the development of cloud-top increased N_{Ice}, and considering the larger particles tended to fall to cloud base and form precipitation, the reduced N_{Ice} close to cloud base may be due to the coalesce of ice which reduced the number but enlarged the size of ice. It should be noted that the observed clouds have included both widespread stratiform and imbedded convective clouds, and the metric of DCT should all apply. The DCT essentially implies the amount of ice hydrometeors may fall from above, but may not be directly associated with updraft strength or turbulence.

N_{Ice} could increase from a few dozens to a few hundreds of numbers per litre, which are all well above the estimation from INP, indicating the strong SIP. For the SIP mechanism, the temperature of P1 (−5 to −8 ºC) was in the typical H-M temperature region, while the temperature of P2 (−12 ºC) was lower than H-M temperature. Even at the same ambient temperature of measurements (because the aircraft penetration was at the same altitude), the N_{Ice} showed a remarkable difference. This suggested the DCT tended to be a more important factor than temperature in determining the intensity of SIP. This could be explained by the seeder-feeder mechanism occurring in the stratiform cloud precipitation (Hobbs and Locatelli, 1978; Hobbs et al., 1980; Matejka et al., 1980): when the cloud-top is higher, more primary ice particles form at colder temperatures and fall. The ice particles can capture smaller liquid water droplets when falling, during which they can grow and the fall speed can be accelerated. This process can considerably enhance the interaction between ice and water droplets, or among ice particles, which is necessary for the occurrence of ice fracture hereby leads to the avalanche secondary ice production. The explanation was also similar to the results reported by Li et al. (2021), which showed the columnar ice crystals were produced in the lower layer seeded by ice particles falling from the upper layer. The age of ice was examined as the fraction of smaller ice ($F_{smaller\ ice}$) here, with the assumption that a youngly formed ice would have smaller size. This implied the pronounced production of smaller ice by SIP processes with $F_{smaller\ ice}$ up to 70% during the developing period, while a lower $F_{smaller,ice}$ (0.2-0.6) indicated the growth of ice and smaller ice was consumed during the dissipating stage. Then the schematic plot of ice production at different stages of clouds was given (Fig. 10). The higher cloud-top leads to the formation of more primary ice through the nucleation process, and the ice can grow in the upper layer and during the falling. The SIP process is triggered when the ice particles in the upper layer fall to the lower layer with supercooled water, initiating the interactions between ice and droplets. In regions with larger DCT, ice particles in the upper layer have sufficient time and distance to grow larger during falling, and the fall speed also can be accelerated, resulting in more and larger ice particles falling to the lower layer. Consequently, the intensity of SIP process becomes stronger in this region because the falling large ice particles enhance the interactions between ice and droplets, as well as among ice particles.

3.4 The production rate of secondary ice

The secondary ice production rate could be estimated through the measured number size distribution of ice (Harris-Hobbs and Cooper, 1987; Crosier et al., 2011). The concentration between the length of 90-140 μm ($N_{90-140\mu m}$) was divided by the time required for ice to grow under this size range. The ice grew linearly under water supersaturation at this size range and was about 1.4 μm/s under T = −6 ºC (Ryan et al., 1976), resulting in around 35.7 s to grow for 50 μm (τ). It was assumed here that the ice numbers were in a steady state that the smaller ice at size (L) = 90 μm grew to L = 140 μm was replenished by smaller ice newly produced purely by splinters. The production rate of the smaller secondary ice could then be estimated by the ice number between this growth size limit ($N_{90-140nm}$) divided by the time required for the growth (τ). Figure S8a showed the measured SIP rate ranged at 0.005-1.8 L^{-1} s^{-1}, generally consisted with previous observations at 0.001-1 L^{-1} s^{-1} for cumulus clouds (Harris-Hobbs and Cooper, 1987), 0.043 L^{-1} s^{-1} for stratus cloud embedded with cumulus (Crosier et al., 2011), 0.14 L^{-1} s^{-1} in the mature region of cumulus (Taylor et al., 2016). Based on the observation data of mixed-phase stratiform cloud system over Northern China, Hou et al. (2021) estimated the SIP rate and found the highest concentration of ice splinter could reach 1000 L^{-1} in five minutes, which implied that the average SIP rate could reach up to 3.3 L^{-1} s^{-1}. Figures S8c and S9 showed the rate was positively correlated with the number concentration of large ice (graupel) and large droplet.

The above analysis showed the importance of collision-coalescence process in producing the enhancement of ice number concentration. The collision-coalescence model had been previously used to calculate the production rate of secondary ice. It was essentially determined by the collision-coalescence between graupel and droplet above certain size. It was long established in the laboratory that only droplet > 25 μm in diameter could produce secondary ice when rimmed on the graupel. The SIP rate could therefore be calculated from the collision-coalescence process among graupel and droplet (Reisner et al., 1998), and the model calculated equation is described as:

$$P = \pi/4 \cdot (D_{graupel} + D_{droplet})^2 N(D_{graupel}) N(D_{droplet}) E |U_{graupel} - U_{droplet}| , \qquad (3)$$

where $D_{graupel}$ and $D_{droplet}$ are the effective diameter (which is the third divided by the second moment of size distribution) of graupel and droplet respectively, and $N(D_{graupel})$ and $N(D_{droplet})$ are the number concentration of graupel and droplet respectively; $U_{graupel}$ and $U_{droplet}$ represent the terminal velocities, which are calculated as the absolute difference between graupel and droplet, as $U_{graupel} = 7 \times 10^2 D_{graupel}$, $U_{droplet} = 3 \times 10^7 D_{droplet}$. E is the collection efficiency among the size bins of graupel and droplet, which was assumed to be 1 for the first instance but would be discussed as follows. The ice particle with $d > 250$ μm was considered as graupel which was able to efficiently capture droplet (Harris-Hobbs and Cooper, 1987). Here the effective radius (Re) was used to represent the size distribution of graupel/droplet within a time window to simplify the calculation of collision among size bins. The Re was used rather than median mass value from the size distribution was because the former was determined by the cross section of particles (and the collection by collision-coalescence process was also determined by area), and weighted towards larger particles. Ice particles were observed to be mostly rimed in images, hereby all ice particles with $d > 250$ μm were considered to be graupels that already accreted by small droplets (i.e. $d < 13$

μm), but not calculated the fraction of rimmed surface (Harris-Hobbs and Cooper, 1987). Considering that the observation here was actually after the SIP process was initialized, when the smaller cloud droplets had been considerably consumed and most ice particles were rimed, the number of large droplets ($d > 50$ μm) was the limited factor for SIP, and therefore used to calculate the modelled SIP rate.

Figure S8a shows the time series of modelled SIP rate, which was well correlated with measured SIP (correlation coefficient was 0.86), the ratio between Re of graupels and large droplets (Re_{Round} / $Re_{Graupel}$) ranged from 0.1-0.8 (Fig. S8b). Figure 11 investigated the correlation between measured and modelled SIP rate, colored by Re_{Round} / $Re_{Graupel}$. According to Eq. (3), the collection efficiency $E = 1$ was firstly considered which gave the upper limit for the calculation, but any other circumstances would cause $E < 1$ and reduced the model results. The model was closed to the observation when Re_{Round} / $Re_{Graupel}$ ranged at 0.4-1 (slope=0.94), but model started to overestimate compared to observation when Re_{Round} / $Re_{Graupel}$ decreased (shown by the datapoints grouped as different levels of Re_{Round} / $Re_{Graupel}$). This clearly indicated reduced E when reduced Re_{Round} / $Re_{Graupel}$. E was then further adjusted to give the modelled SIP rate matched with observation at different levels of Re_{Round} / $Re_{Graupel}$, shown in the sub-plot of Fig. 11. A linearly increased collection efficiency was found, when E increased from 0.2 to 1 with Re_{Round} / $Re_{Graupel}$ increased from 0.1 to 0.7. This was consisted with the theory of droplet collision, when the collector particle approaches the droplet, the droplet tends to follow the streamline around the collector particle and may avoid collision (Wallace and Hobbs, 2006; Pruppacher and Klett, 2010). The collision efficiency was small when the collector particle was much larger than the droplet, because too small particles would follow the streamline around collector particle due to small inertia, and the collision efficiency increased with increased droplet size because droplets with greater inertia tended to follow a straight line. The results here implied that the SIP rate could be well explained by the collision theory between graupel and large droplet, and the availability of both numbers and the chance for their collision were the factors in determining the SIP rate.

4 Conclusion

In this study, we investigated the ice production of stratiform clouds with embedded convection during an extratropical cyclone over the North China Plain, through in-situ measurements of the microphysical properties. The aircraft penetrated four stages during the lifecycle of the clouds including the developing, mature, dissipating and young cells. The four relative stages were identified by ice mass fraction, by considering a more mature cloud has a more glaciated fraction. In developing cells, high N_{Ice} and LWC-rich region were observed, the ice mass fraction in clouds spanned from zero (pure water) to unit (pure ice). In mature cells, a higher glaciation extent was observed, with ice mass fraction ranging from 0.36 to 1, and N_{Ice} reaching up to 300 L^{-1} at this stage. The dissipating cells were dominated by ice but only intermittent unglaciated LWC-rich clouds, and the ice mass fraction ranged in 0.56-1. The young stage was rich of LWC with lower ice mass fraction. The number concentration of ice was found to frequently well exceeds that from ice nucleation, reaching up to a few hundred per litre, indicating the strong secondary ice production (SIP).

The seeder-feeder process was found to extend the SIP process beyond the slightly supercooled temperature region for the typically considered H-M process. The intensity of SIP was to the first order determined by the numbers of graupel and droplets, because the collision and coalescence among these hydrometeors necessitated the fracture of ice. The modelled and measurement-based calculations showed appropriately treating the size distribution hereby the determination of collection efficiency will improve the modelling of the SIP rate. Importantly, the results showed the generally enhanced SIP when larger distance to cloud-top, which means once the cloud-top reached sufficient height, the initialized ice from nucleation may boost the avalanche glaciation process when falling ice reached lower levels in cloud. It should be noted that whether the falling hydrometeors were the ones generated by the ice production process or were about to participate in the ice production process at the same level, may never be separated due to the short time-scale of the collision process. However, this is a continuous process which may involve both the already-formed and ongoing-happening particles, and the observed or modelled results are an overall net production of ice. The ice particles falling from aloft increase the numbers of graupels and collision chance between graupel and droplets, and then trigger the SIP process, therefore the seeder-feeder and SIP process may occur simultaneously after SIP process has initialized. The results about the microphysical properties of stratiform clouds with convective cells under different stages suggest the falling hydrometeors associated with cloud-top height importantly controlled the cloud glaciation and precipitation process, and this may also help find the region of supercooled water of clouds for the weather modification work.

Data availability

420 The data in this study are available from the authors upon request.

Author contribution

YD and DL analyzed the data and wrote the manuscript, and this work was completed under the guidance of DL, MH and DD. DeZ, PT, WX, WZ, JS and FW contributed to the aircraft data processing and analysis. DW, XL and YC performed the

425 synoptic analysis. BP, YJ contributed to the satellite data analysis. DoZ and YH contributed to the radar data processing and analysis. RZ conducted the shape classification of 2D-S images.

Competing interests

At least one of the (co-)authors is a member of the editorial board of *Atmospheric Chemistry* and *Physics*. The authors also

430 have no other competing interests to declare.

Acknowledgements

This research was supported by the National Natural Science Foundation of China (Grant Nos. 42205093, 42075084, 42005078).

435

440

445

450 References

Bacer, S., Sullivan, S. C., Sourdeval, O., Tost, H., Lelieveld, J., and Pozzer, A.: Cold cloud microphysical process rates in a global chemistry–climate model, Atmospheric Chemistry and Physics, 21, 1485-1505, 10.5194/acp-21-1485-2021, 2021.

Beswick, K. M., Gallagher, M. W., Webb, A. R., Norton, E. G., and Perry, F.: Application of the Aventech AIMMS20AQ airborne probe for turbulence measurements during the Convective Storm Initiation Project, Atmospheric Chemistry and Physics, 8, 5449-5463, 2008.

455 Cai, Y., Snider, J. R., and Wechsler, P.: Calibration of the passive cavity aerosol spectrometer probe for airborne determination of the size distribution, Atmospheric Measurement Techniques, 6, 2349-2358, 10.5194/amt-6-2349-2013, 2013.

Cantrell, W. and Heymsfield, A.: Production of Ice in Tropospheric Clouds: A Review, Bulletin of the American Meteorological Society, 86, 795-808, 10.1175/bams-86-6-795, 2005.

Crosier, J., Choularton, T. W., Westbrook, C. D., Blyth, A. M., Bower, K. N., Connolly, P. J., Dearden, C., Gallagher, M. W., Cui, Z., and
460 Nicol, J. C.: Microphysical properties of cold frontal rainbands†, Quarterly Journal of the Royal Meteorological Society, 140, 1257-1268, 10.1002/qj.2206, 2013.

Crosier, J., Bower, K. N., Choularton, T. W., Westbrook, C. D., Connolly, P. J., Cui, Z. Q., Crawford, I. P., Capes, G. L., Coe, H., Dorsey, J. R., Williams, P. I., Illingworth, A. J., Gallagher, M. W., and Blyth, A. M.: Observations of ice multiplication in a weakly convective cell embedded in supercooled mid-level stratus, Atmospheric Chemistry and Physics, 11, 257-273, 10.5194/acp-11-257-2011, 2011.

465 DeMott, P. J., Prenni, A. J., Liu, X., Kreidenweis, S. M., Petters, M. D., Twohy, C. H., Richardson, M. S., Eidhammer, T., and Rogers, D. C.: Predicting global atmospheric ice nuclei distributions and their impacts on climate, Proc Natl Acad Sci U S A, 107, 11217-11222, 10.1073/pnas.0910818107, 2010.

Field, P. R., Lawson, R. P., Brown, P. R. A., Lloyd, G., Westbrook, C., Moisseev, D., Miltenberger, A., Nenes, A., Blyth, A., Choularton, T., Connolly, P., Buehl, J., Crosier, J., Cui, Z., Dearden, C., DeMott, P., Flossmann, A., Heymsfield, A., Huang, Y., Kalesse, H., Kanji, Z.
470 A., Korolev, A., Kirchgaessner, A., Lasher-Trapp, S., Leisner, T., McFarquhar, G., Phillips, V., Stith, J., and Sullivan, S.: Secondary Ice Production - current state of the science and recommendations for the future, Meteorological Monographs, 10.1175/amsmonographs-d-16-0014.1, 2016.

Gurganus, C. and Lawson, P.: Laboratory and Flight Tests of 2D Imaging Probes: Toward a Better Understanding of Instrument Performance and the Impact on Archived Data, Journal of Atmospheric and Oceanic Technology, 35, 1533-1553, 10.1175/jtech-d-17-
475 0202.1, 2018.

Hallett, J. and Mossop, S. C.: Production of Secondary ice particles during the riming process, Nature, 249, 26–28, doi:10.1038/249026a0., 1974.

Harris-Hobbs, R. L. and Cooper, W. A.: Field evidence supporting quantitative predictions of secondary ice production rates, journal of the atmospheric sciences, 44, 1071-1082, 1987.

480 Hobbs, P. V. and Locatelli, J. D.: Rainbands, Precipitation Cores and Generating Cells in a Cyclonic Storm, Journal of Atmospheric Sciences, 35, 230-241, 1978.

Hobbs, P. V., Matejka, T. J., Herzegh, P. H., Locatelli, J. D., and Houze , R. A.: The Mesoscale and Microscale Structure and Organization of Clouds and Precipitation in Midlatitude Cyclones. I: A Case Study of a Cold Front, Journal of Atmospheric Sciences, 37, 568-596, 1980.

Hogan, R. J., Field, P. R., Illingworth, A. J., Cotton, R. J., and Choularton, T. W.: Properties of embedded convection in warm-frontal
485 mixed-phase cloud from aircraft and polarimetric radar, Quarterly Journal of the Royal Meteorological Society: A journal of the atmospheric sciences, applied meteorology and physical oceanography, 128, 451-476, 2002.

Holroyd, E. W.: Some Techniques and Uses of 2D-C Habit Classification Software for Snow Particles, Journal of Atmospheric and Oceanic Technology, 4, 498–511, 1987.

Hou, T., Lei, H., He, Y., Yang, J., Zhao, Z., and Hu, Z.: Aircraft Measurements of the Microphysical Properties of Stratiform Clouds with
490 Embedded Convection, Advances in Atmospheric Sciences, 38, 966-982, 10.1007/s00376-021-0287-8, 2021.

Hou, T., Chen, B., Zhou, X., Zhao, C., Feng, Q., Yan, F., Zhou, W., Cui, Y., Du, Y., Li, Z., Zhao, D., and Ma, X.: Aircraft-based observations of ice concentrations in a midlatitude mixed-phase stratiform cloud system with embedded convection, Atmospheric Research, 281, 10.1016/j.atmosres.2022.106471, 2023.

Huang, Y., Blyth, A. M., Brown, P. R. A., Choularton, T. W., Connolly, P., Gadian, A. M., Jones, H., Latham, J., Cui, Z., and Carslaw, K.:
495 The development of ice in a cumulus cloud over southwest England, New Journal of Physics, 10, 10.1088/1367-2630/10/10/105021, 2008.

Jiang, Y. and Liu, L.: A test pattern identification algorithm and its application to CINRAD/SA(B) data, Advances in Atmospheric Sciences, 31, 331-343, 10.1007/s00376-013-2315-9, 2014.

Kanji, Z. A., Ladino, L. A., Wex, H., Boose, Y., Burkert-Kohn, M., Cziczo, D. J., and Krämer, M.: Overview of Ice Nucleating Particles, Meteorological Monographs, 58, 1.1-1.33, 10.1175/amsmonographs-d-16-0006.1, 2017.

500 Korolev, A. and Isaac, G. A.: Relative humidity in liquid, mixed-phase, and ice clouds., Journal of the atmospheric sciences, 63, 2865-2880, 2006.

Korolev, A., DeMott, P. J., Heckman, I., Wolde, M., Williams, E., Smalley, D. J., and Donovan, M. F.: Observation of secondary ice production in clouds at low temperatures, Atmospheric Chemistry and Physics, 22, 13103-13113, 10.5194/acp-22-13103-2022, 2022.

Korolev, A., Heckman, I., Wolde, M., Ackerman, A. S., Fridlind, A. M., Ladino, L. A., Lawson, R. P., Milbrandt, J., and Williams, E.: A new look at the environmental conditions favorable to secondary ice production, Atmospheric Chemistry and Physics, 20, 1391-1429, 10.5194/acp-20-1391-2020, 2020.

Korolev, A., McFarquhar, G., Field, P. R., Franklin, C., Lawson, P., Wang, Z., Williams, E., Abel, S. J., Axisa, D., Borrmann, S., Crosier, J., Fugal, J., Krämer, M., Lohmann, U., Schlenczek, O., Schnaiter, M., and Wendisch, M.: Mixed-Phase Clouds: Progress and Challenges, Meteorological Monographs, 58, 5.1-5.50, 10.1175/amsmonographs-d-17-0001.1, 2017.

Lance, S., Brock, C. A., Rogers, D., and Gordon, J. A.: Water droplet calibration of the Cloud Droplet Probe (CDP) and in-flight performance in liquid, ice and mixed-phase clouds during ARCPAC, Atmospheric Measurement Techniques, 3, 1683-1706, 10.5194/amt-3-1683-2010, 2010.

Lau, K. M. and Wu, H. T.: Warm rain processes over tropical oceans and climate implications, Geophysical Research Letters, 30, 10.1029/2003gl018567, 2003.

Lawson, R. P. and Cooper, W. A.: Performance of some airborne thermometers in clouds, Journal of Atmospheric and Oceanic Technology, 7, 480–494, 10.1175/1520-0426(1990)007,0480:POSATI.2.0.CO;2, 1990.

Lawson, R. P. and Rodi, A. R.: A New Airborne Thermometer for Atmospheric and Cloud Physics Research. Part I: Design and Preliminary Flight Tests, Journal of Atmospheric and Oceanic Technology, 9, 556-574, 1992.

Lawson, R. P., Stewart, R. E., and Angus, L. J.: Observations and Numerical Simulations of the Origin and Development of Very Large Snowflakes, Journal of the Atmospheric Sciences, 55, 1998.

Lawson, R. P., Woods, S., and Morrison, H.: The Microphysics of Ice and Precipitation Development in Tropical Cumulus Clouds, Journal of the Atmospheric Sciences, 72, 2429-2445, 10.1175/jas-d-14-0274.1, 2015.

Lawson, R. P., O'Connor, D., Zmarzly, P., Weaver, K., Baker, B., Mo, Q., and Jonsson, H.: The 2D-S (Stereo) Probe: Design and Preliminary Tests of a New Airborne, High-Speed, High-Resolution Particle Imaging Probe, Atmospheric and Oceanic Technology, 23, 1462–1477, 2006.

Lenschow, D. H. and Pennell, W. T.: On the measurement of in-cloud and wet-bulb temperatures from an aircraft, Monthly Weather Review, 102, 447-454, 1974.

Li, H., Möhler, O., Petäjä, T., and Moisseev, D.: Two-year statistics of columnar-ice production in stratiform clouds over Hyytiälä, Finland: environmental conditions and the relevance to secondary ice production, Atmospheric Chemistry and Physics, 21, 14671-14686, 10.5194/acp-21-14671-2021, 2021.

Li, Z., Lau, W. K. M., Ramanathan, V., Wu, G., Ding, Y., Manoj, M. G., Liu, J., Qian, Y., Li, J., Zhou, T., Fan, J., Rosenfeld, D., Ming, Y., Wang, Y., Huang, J., Wang, B., Xu, X., Lee, S. S., Cribb, M., Zhang, F., Yang, X., Zhao, C., Takemura, T., Wang, K., Xia, X., Yin, Y., Zhang, H., Guo, J., Zhai, P. M., Sugimoto, N., Babu, S. S., and Brasseur, G. P.: Aerosol and monsoon climate interactions over Asia, Reviews of Geophysics, 54, 866-929, 10.1002/2015rg000500, 2016.

Liu, Q., Liu, D., Gao, Q., Tian, P., Wang, F., Zhao, D., Bi, K., Wu, Y., Ding, S., Hu, K., Zhang, J., Ding, D., and Zhao, C.: Vertical characteristics of aerosol hygroscopicity and impacts on optical properties over the North China Plain during winter, Atmospheric Chemistry and Physics, 20, 3931-3944, 10.5194/acp-20-3931-2020, 2020.

Lloyd, G., Dearden, C., Choularton, T. W., Crosier, J., and Bower, K. N.: Observations of the Origin and Distribution of Ice in Cold, Warm, and Occluded Frontal Systems during the DIAMET Campaign, Monthly Weather Review, 142, 4230-4255, 10.1175/mwr-d-13-00396.1, 2014.

Locatelli, J. D., Stoelinga, M. T., and Woods, C. P.: Size Spectra of Snow Particles Measured in Wintertime Precipitation in the Pacific Northwest, Journal of the Atmospheric Sciences, 65, 189-205, 10.1175/2007jas2243.1, 2008.

Lohmann, U. and Feichter, J.: Global indirect aerosol effects: a review, Atmos. Chem. Phys., 5, 715–737, https://doi.org/10.5194/acp-5-715-2005, 2005.

Lu, C., Liu, Y., Niu, S., and Vogelmann, A. M.: Observed impacts of vertical velocity on cloud microphysics and implications for aerosol indirect effects, Geophysical Research Letters, 39, 10.1029/2012gl053599, 2012.

Matejka, T. J., Houze, R. A., and Hobbs, P. V.: Microphysics and dynamics of clouds associated with mesoscale rainbands in extratropical cyclones, Quarterly Journal of the Royal Meteorological Society, 106, 29–56, 10.1002/qj.49710644704 1980.

McFarquhar, G. M., Baumgardner, D., and Heymsfield, A. J.: Background and Overview, Meteorological Monographs, 58, v-ix, 10.1175/amsmonographs-d-16-0018.1, 2017.

Mossop, S. C.: Secondary ice particle production during rime growth: The effect of drop size distribution and rimer velocity, Quarterly Journal of the Royal Meteorological Society, 111, 1113-1124, 1985.

Mülmenstädt, J., Sourdeval, O., Delanoë, J., and Quaas, J.: Frequency of occurrence of rain from liquid-, mixed-, and ice-phase clouds derived from A-Train satellite retrievals, Geophysical Research Letters, 42, 6502-6509, 10.1002/2015gl064604, 2015.

Pruppacher, H. R. and Klett, J. D.: Microphysics of Clouds and Precipitation, Springer2010.

Rangno, A. L. and Hobbs, P. V.: Ice particles in stratiform clouds in the Arctic and possible mechanisms for the production of high ice concentrations, Journal of Geophysical Research: Atmospheres, 106, 15065-15075, 10.1029/2000jd900286, 2001.

Reisner, J., Rasmussen, R. M., and Bruintjes, R. T.: Explicit forecasting of supercooled liquid water in winter storms using the MM5 mesoscale model, Quarterly Journal of the Royal Meteorological Society, 124, 1071–1107, https://doi.org/10.1002/qj.49712454804, 1998.

560   Ryan, B. F., Wishart, E. R., and Shaw, D. E.: Growth Rates and Densities of Ice Crystals between −3°C and −21°C, Journal of Atmospheric Sciences, 33, 842-850, 1976.

Taylor, J. W., Choularton, T. W., Blyth, A. M., Liu, Z., Bower, K. N., Crosier, J., Gallagher, M. W., Williams, P. I., Dorsey, J. R., Flynn, M. J., Bennett, L. J., Huang, Y., French, J., Korolev, A., and Brown, P. R. A.: Observations of cloud microphysics and ice formation during COPE, Atmospheric Chemistry and Physics, 16, 799-826, 10.5194/acp-16-799-2016, 2016.

565   Tian, P., Liu, D., Zhao, D., Yu, C., Liu, Q., Huang, M., Deng, Z., Ran, L., Wu, Y., Ding, S., Hu, K., Zhao, G., Zhao, C., and Ding, D.: In situ vertical characteristics of optical properties and heating rates of aerosol over Beijing, Atmospheric Chemistry and Physics, 20, 2603-2622, 10.5194/acp-20-2603-2020, 2020.

Wallace, J. M. and Hobbs, P. V.: Atmospheric Science: An Introductory Survey, Elsevier2006.

Wang, D., Duan, Y., Liu, Y., Liang, Z., Liu, C., Zhao, Y., Zhang, Y., Yin, J., and Wang, H.: A case study of the November 2012 mixed
570   rain-snow storm over North China, Acta Meteorologica Sinica, 27, 601-625, 10.1007/s13351-013-0512-1, 2014.

Woods, S., Lawson, R. P., Jensen, E., Bui, T. P., Thornberry, T., Rollins, A., Pfister, L., and Avery, M.: Microphysical Properties of Tropical Tropopause Layer Cirrus, Journal of Geophysical Research: Atmospheres, 123, 6053-6069, 10.1029/2017jd028068, 2018.

Yang, J., Lei, H., and Hou, T.: Observational evidence of high ice concentration in a shallow convective cloud embedded in stratiform cloud over North China, Advances in Atmospheric Sciences, 34, 509-520, 10.1007/s00376-016-6079-x, 2017.

575   Zhang, R., Li, H., Zhou, X., Li, H., Hu, X., and Xia, Q.: Shape Recognition of DMT Airborne Cloud Particle Images and Its Application, JOURNAL OF APPLIED METEOROLOGICAL SCIENCE 32, 735-747, 10.11898/1001-7313.20210608, 2021.

Zhao, C., Chen, Y., Li, J., Letu, H., Su, Y., Chen, T., and Wu, X.: Fifteen-year statistical analysis of cloud characteristics over China using Terra and Aqua Moderate Resolution Imaging Spectroradiometer observations, International Journal of Climatology, 39, 2612-2629, 10.1002/joc.5975, 2019.

580   Zuo, D., Liu, D., Zhao, D., Yang, L., Chen, Y., Zhou, W., Huang, M., He, H., Tian, P., Du, Y., Xiao, W., Li, R., Li, J., Gao, Y., Lu, J., Tang, Q., Wang, W., and Ding, D.: Liquid water determination by airborne millimeter cloud radar and in-situ size distribution measurements, Atmospheric Research, 284, 10.1016/j.atmosres.2023.106607, 2023.

585
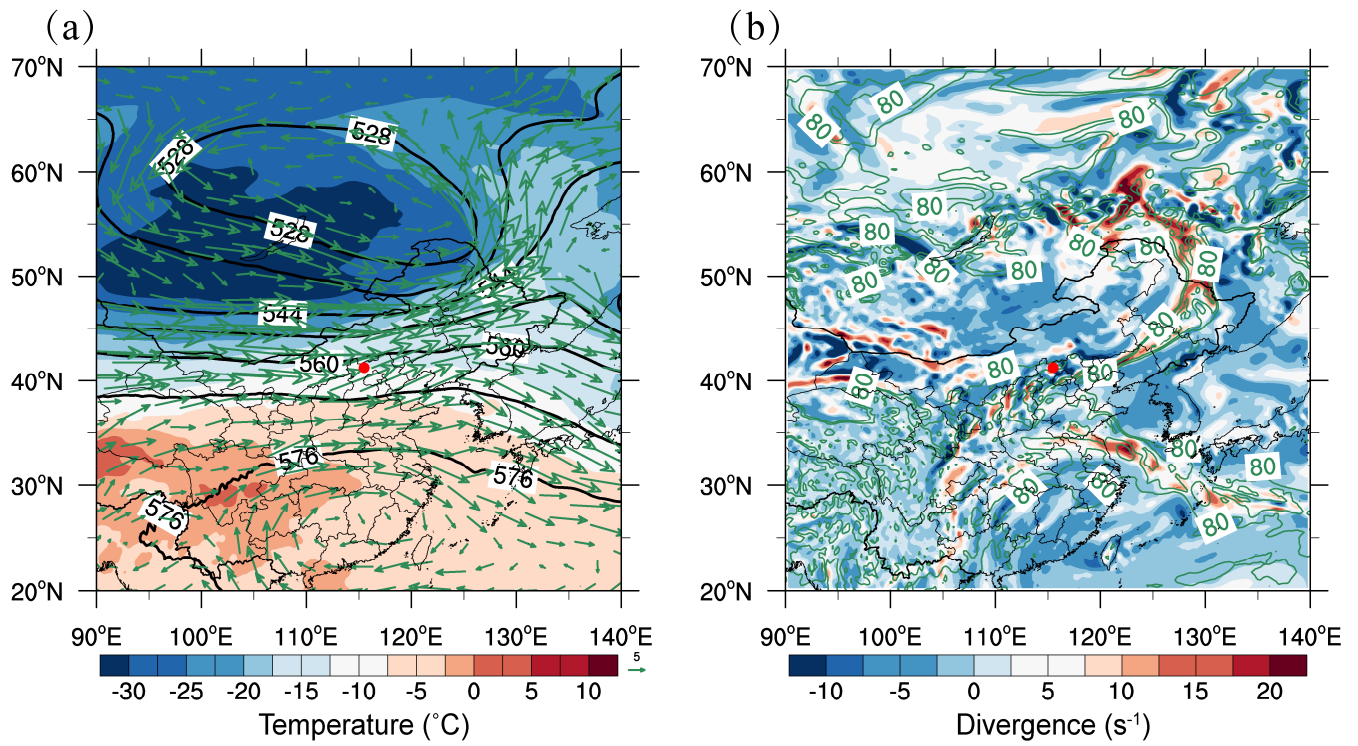
590   **Figure 1: Synoptic overview during experiment. (a) The 500hPa temperature (color), height field (contour), wind field (arrow) at 08:00 (UTC+8h) on September 26th, 2017; (b) 850hPa divergence field (color), relative humidity (green line, only >80% is shown). The experimental region is indicated by the red dot on each plot.**

595

600
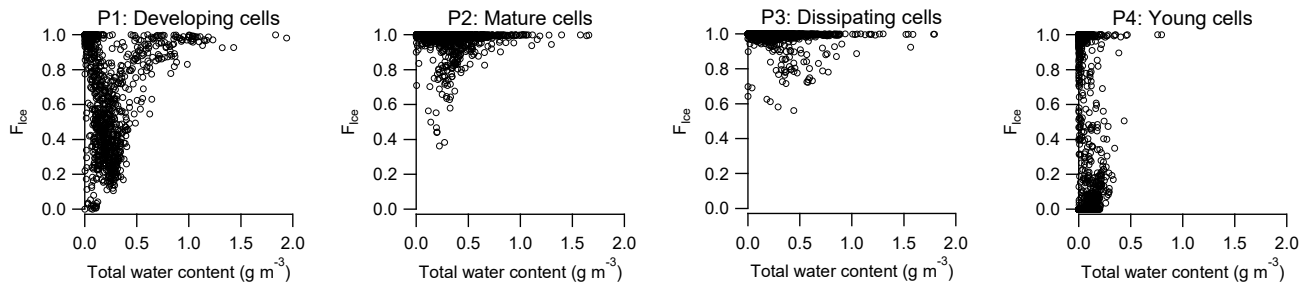
605 **Figure 2: Ice mass fraction (F_{Ice}) as a fuction of total water content at four stages.**

610

615

620
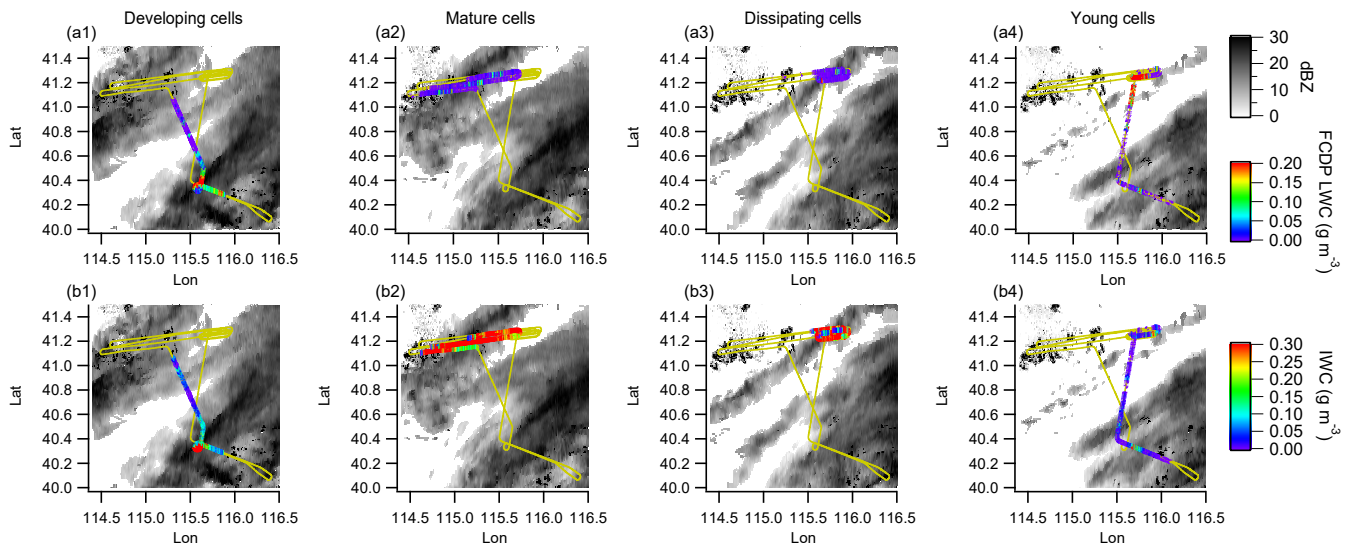
625

Figure 3: Flight tracks mapping on the composite reflectivity of S-band precipitation radar at different stages of clouds (from left to right). (a) colored by liquid water content (LWC) from the FCDP, (b) colored by ice water content (IWC) from the 2D-S.

630

635

640
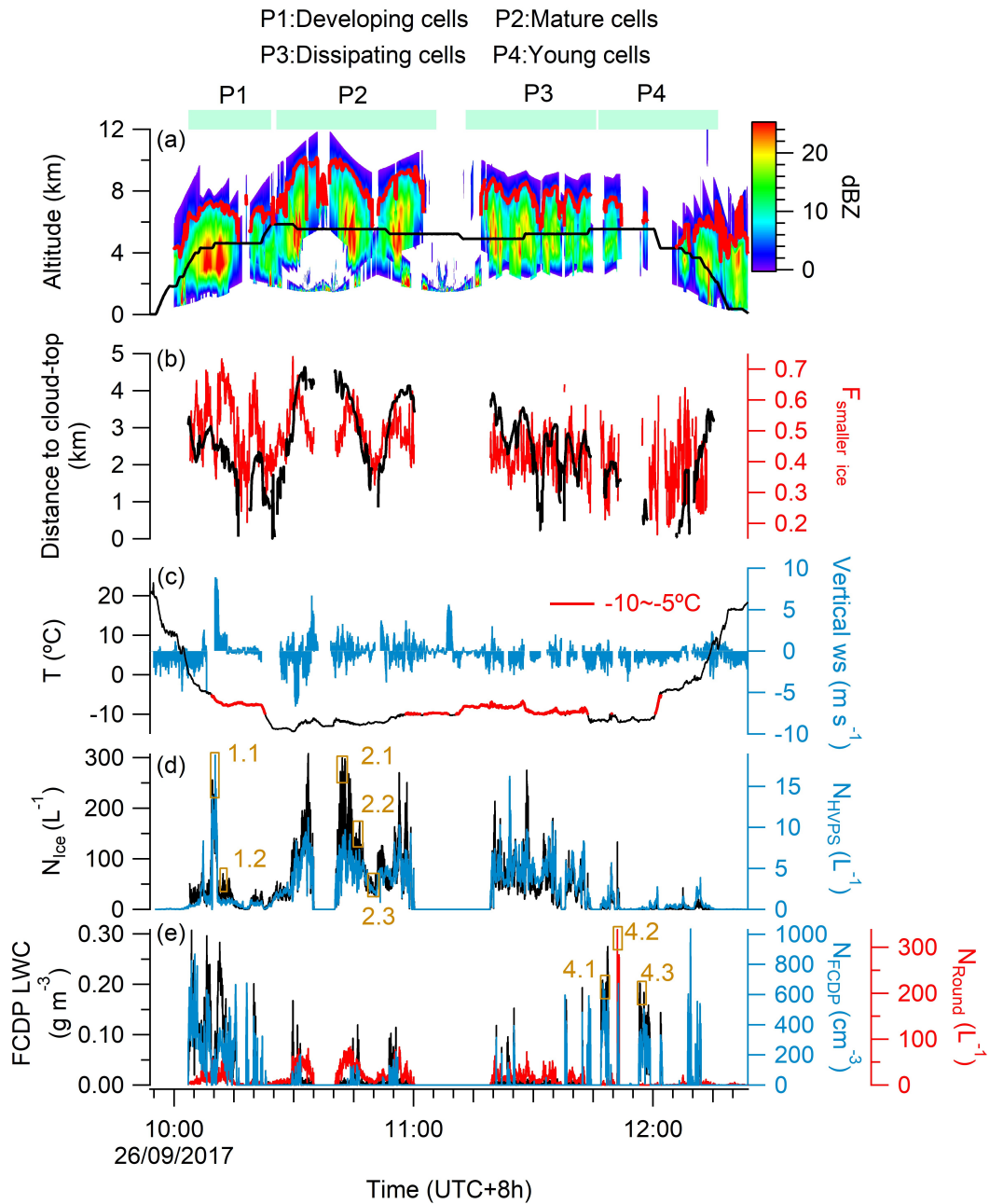
Figure 4: Time series of key cloud properties along the flight track. (a) Vertical profile of radar reflectivity from the ground S-band precipitation radar collocating with the flight path. (b)The distance to cloud-top of aircraft and smaller ice (d < 180 μm) number fraction ($F_{smaller\ ice}$). (c) Ambient temperature and vertical wind speed. (d) Ice number concentration (N_{Ice}) from the 2D-S and precipitation particle number concentration (N_{HVPS}) from the HVPS. (e) LWC and cloud droplet number concentration (N_{FCDP}) from the FCDP, and the large droplet number concentration (N_{Round}) from the 2D-S. The targeting periods are indexed for further analysis.
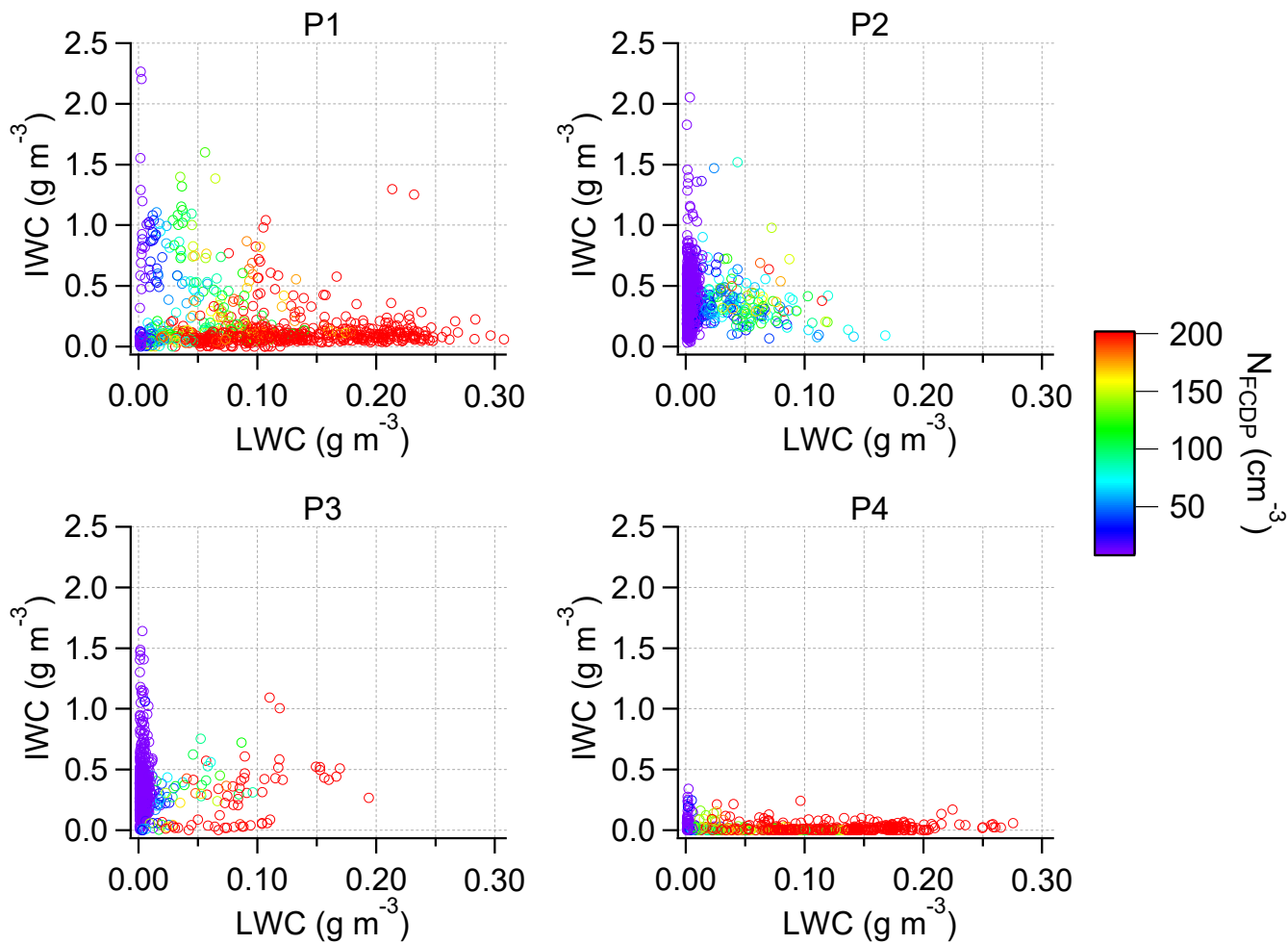
Figure 5: LWC as a function of IWC at different stages of clouds, colored by N_{FCDP}.

655

660
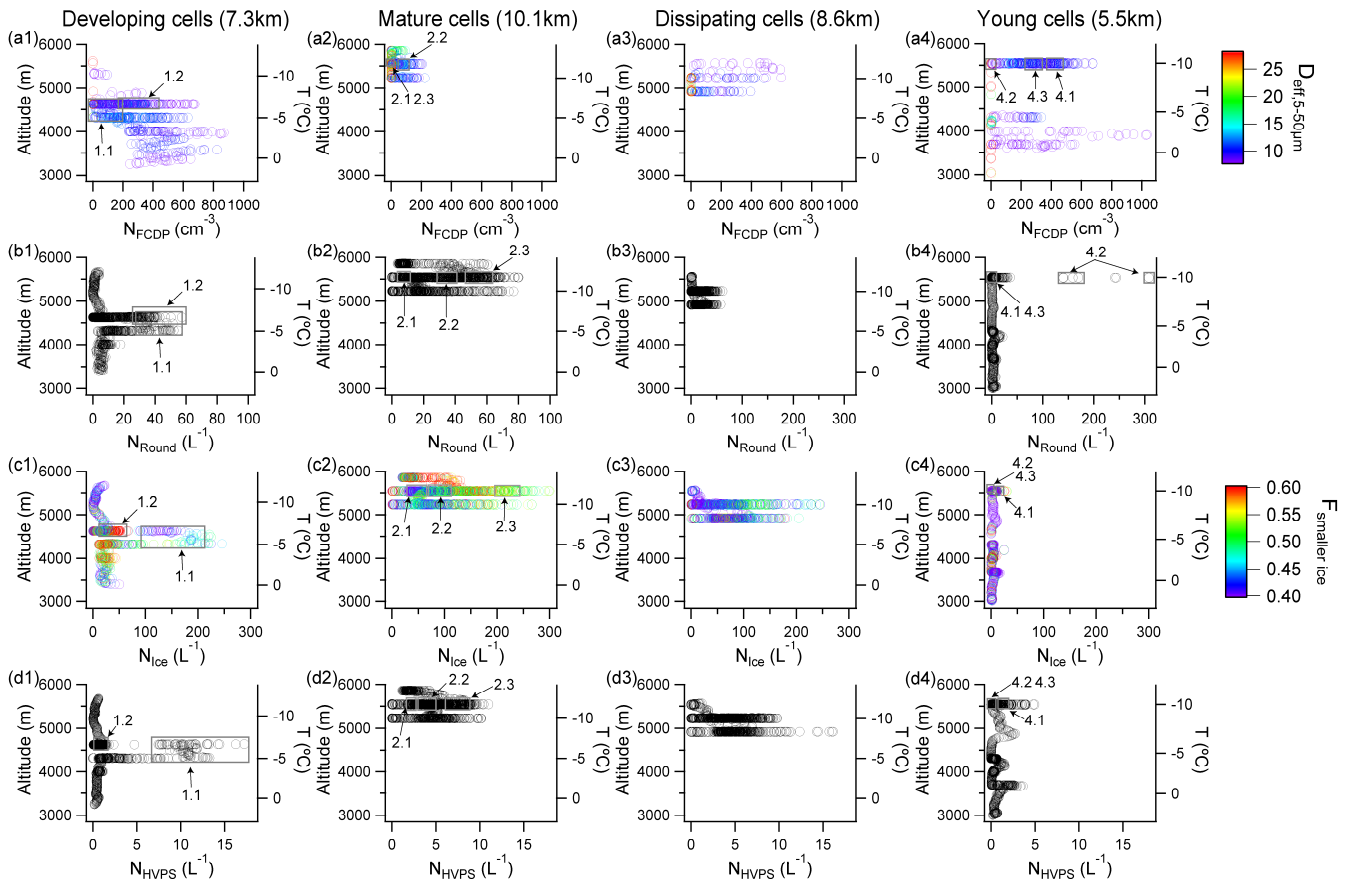
Figure 6: Vertical distributions of hydrometeors at different stages of clouds. (a) N_{FCDP} **colored by the effective diameter of droplet (5-50 μm), (b)** N_{Round}**, (c)** N_{Ice} **colored by** $F_{smaller\ ice}$**, (d)** N_{HVPS}**. The corresponding indexed events in timeseries are marked in this**
665 **figure, and the cloud-top height was indicated in title brackets.**

670

675
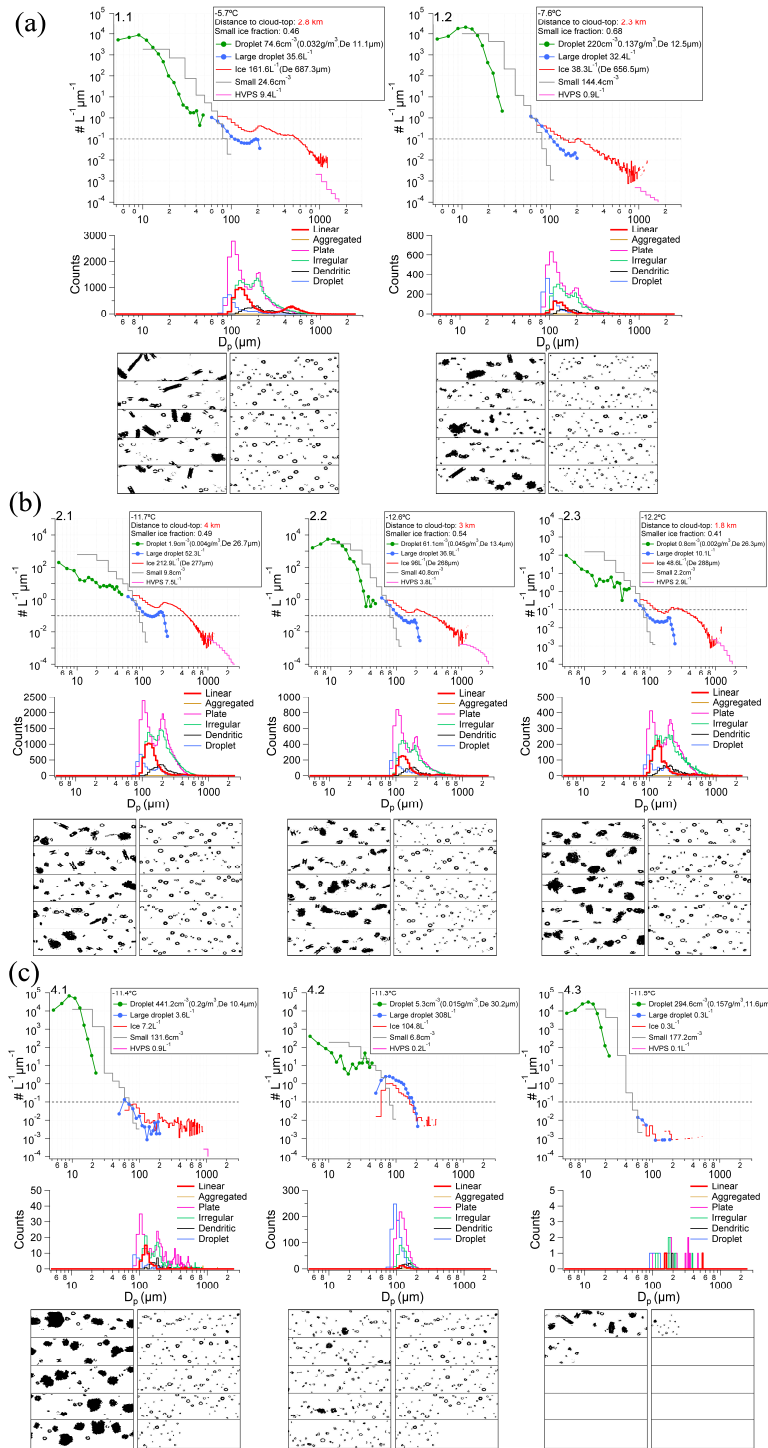
Figure 7: Particle size spectrum from airborne particle spectrum probes, the 2D-S images and the shape classification results of 2D-S images (a) periods 1.1 and 1.2, (b) periods 2.1, 2.2 and 2.3, (c) periods 4.1, 4.2 and 4.3.
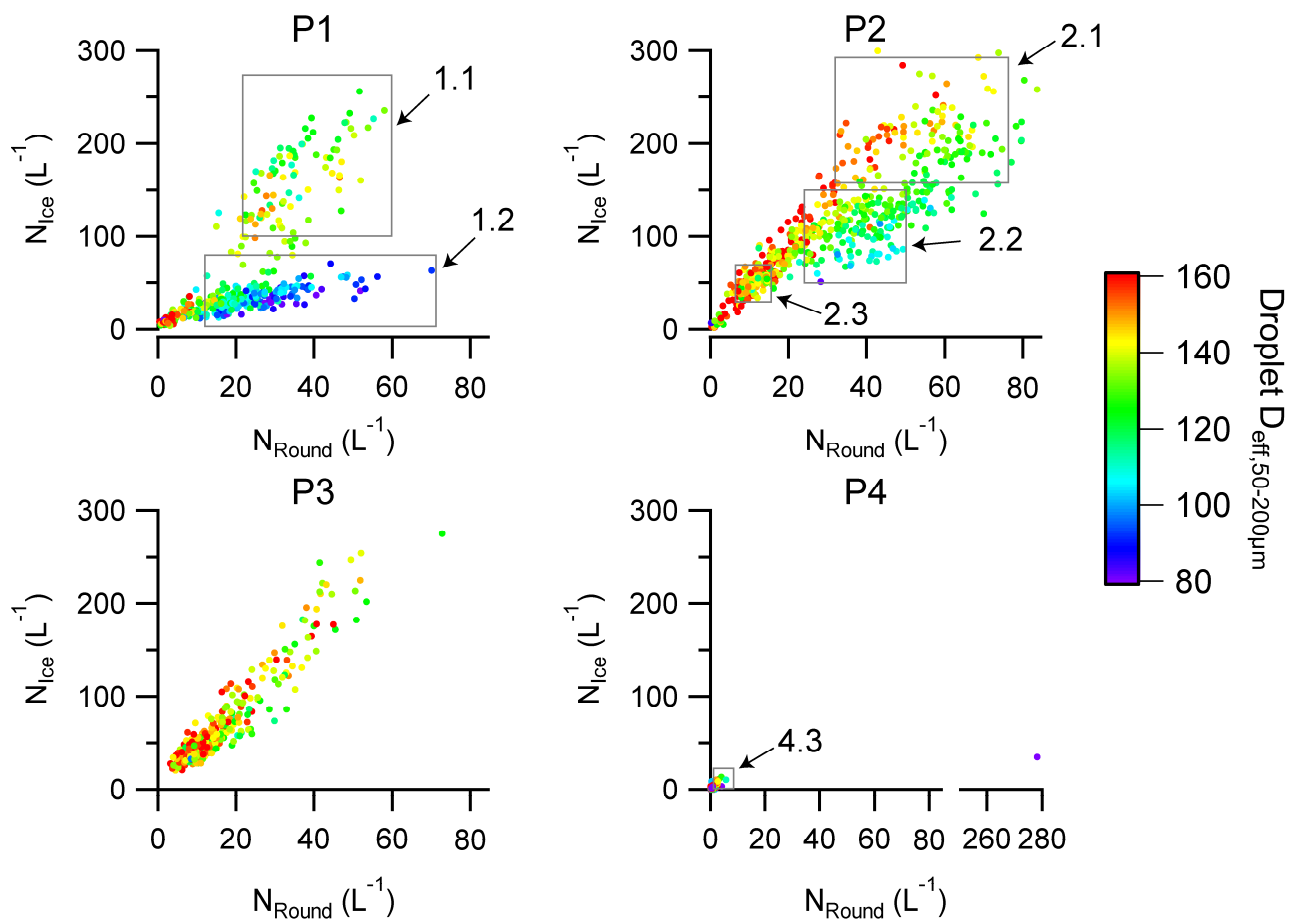
680

Figure 8: N_{Round} as a function of N_{Ice} at different stages, colored by the diameter of large droplet (50-200 μm).

685

690
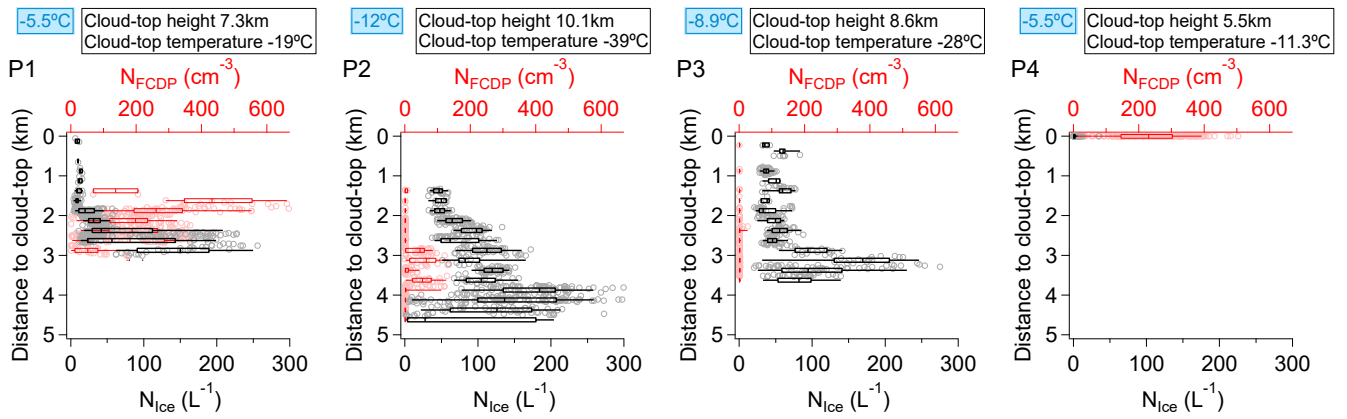
Figure 9: N_{FCDP} and N_{Ice} as a function of distance to cloud-top. Gray circled markers and black boxes represent N_{Ice}, light red circled markers and red boxes represent N_{FCDP}. Whiskers extend to 5th and 95th percentiles, boxes encompass 25th to 75th percentiles and 50th percentiles are vertical lines. The blue box in each figure indicates the temperature of aircraft measurements.

715
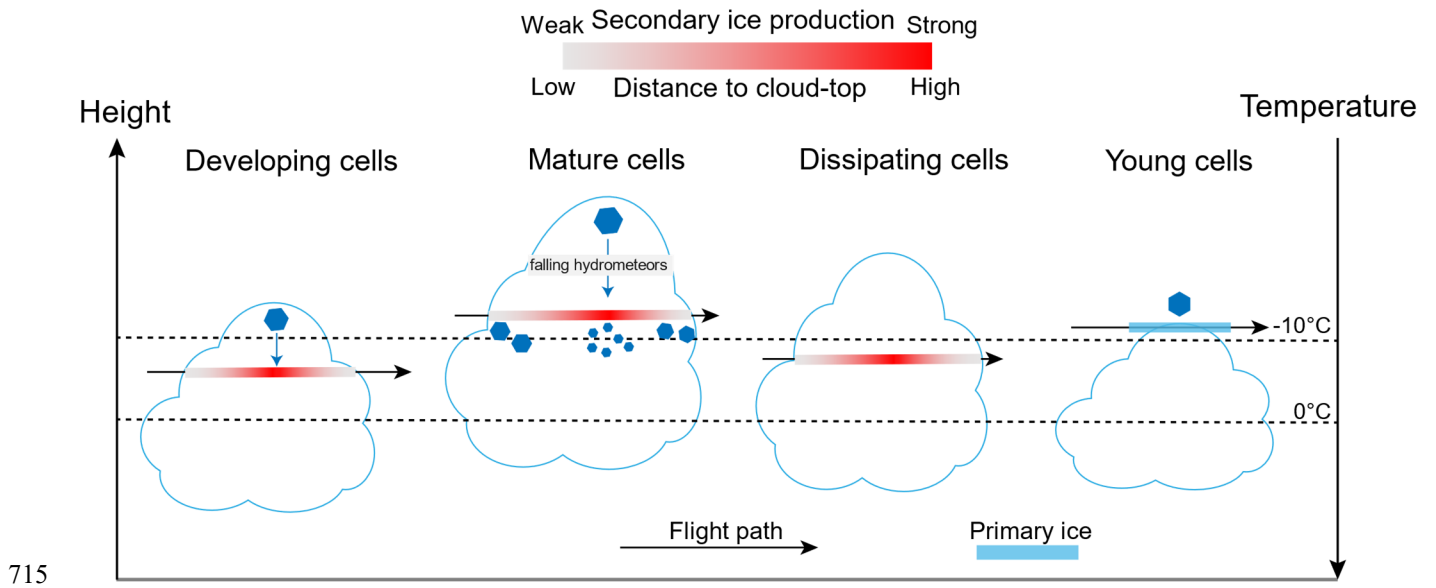
Figure 10: Schematic show of ice production at different stages of clouds.

720

725

730
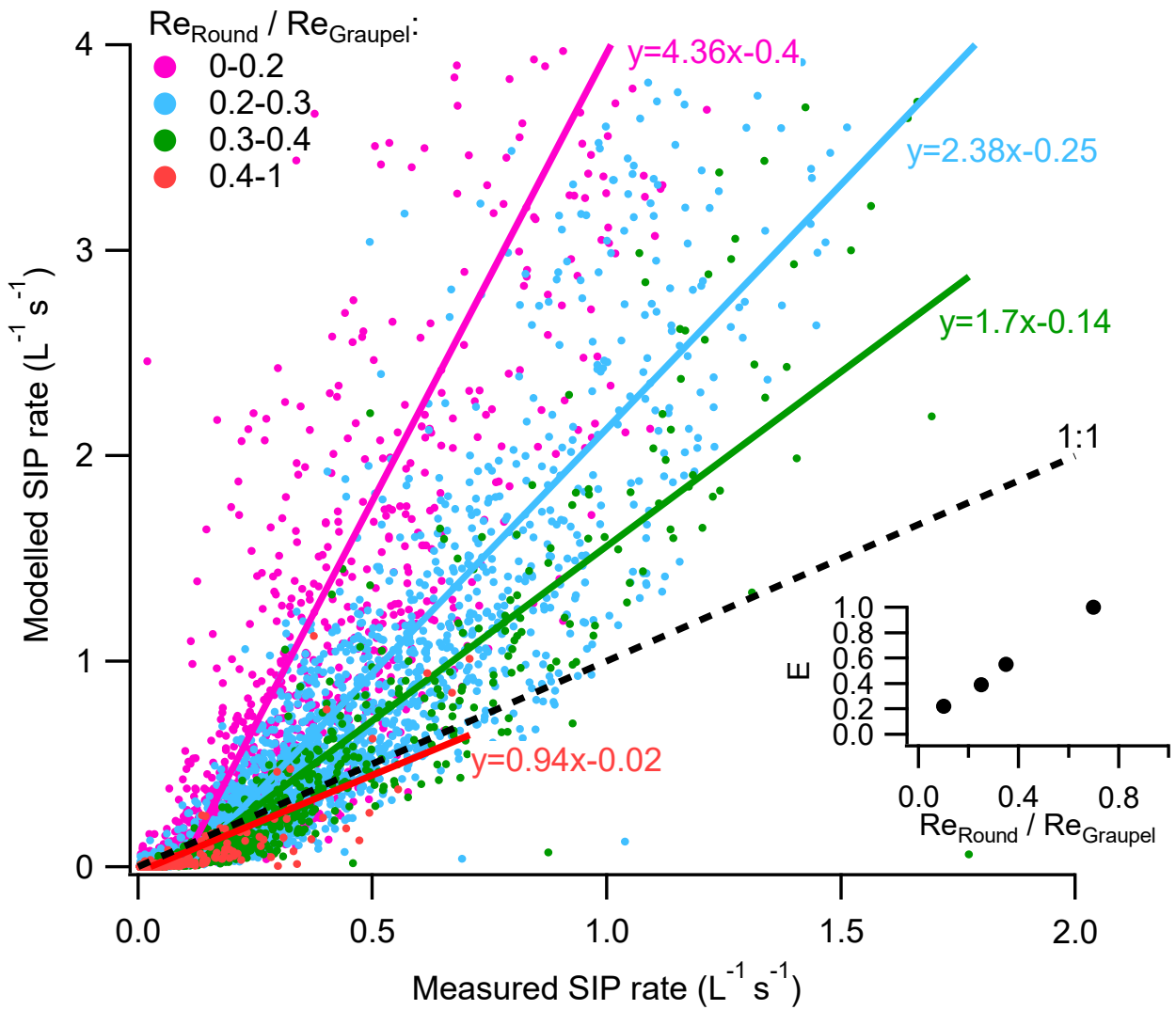
735

Figure 11: Measured against modelled secondary ice production (SIP) rate. The scatter plot is classified and colored by the ratio of effective radius between large droplet and graupel (Re$_{Round}$ / Re$_{graupel}$), and each group of data points is performed least-square linear fitting. The sub-plot shows the derived collection efficiency between graupel and large droplet at different Re$_{Round}$ / Re$_{graupel}$.

740